

Skyrmionic Spin Structures in Layered Fe_5GeTe_2 Up To Room Temperature

Maurice Schmitt¹, Thibaud Denneulin², András Kovács², Tom G. Saunderson¹, Philipp Rüßmann^{3, 4}, Aga Shahee¹, Tanja Scholz⁵, Amir Tavabi², Martin Gradhand⁶, Phivos Mavropoulos⁷, Bettina Lotsch⁵, Yuriy Mokrousov⁴, Stefan Blügel⁴, and Mathias Kläui^{1, 8}

¹Johannes Gutenberg Universität Mainz, Institut für Physik,
Staudingerweg 7, 55128 Mainz, Germany

²Ernst Ruska Centre for Microscopy and Spectroscopy with
Electrons and Peter Grünberg Institute, Forschungszentrum Jülich,
52425 Jülich, Germany

³Institute of Theoretical Physics and Astrophysics, University of
Würzburg, Am Hubland, 97074 Würzburg, Germany

⁴Peter Grünberg Institut and Institute for Advanced Simulation,
Forschungszentrum Jülich, 52425 Jülich, Germany

⁵Max Planck Institute for Solid State Research, Heisenbergstraße
1, 70569 Stuttgart, Germany

⁶University of Bristol, School of Physics, HH Wills Physics
Laboratory, Tyndall Avenue, Bristol BS8 1TL, England

⁷National and Kapodistrian University of Athens, Department of
Physics, University Campus, GR-157 84 Zografou, Athens

⁸Norwegian University of Science and Technology, Department of
Physics, NTNU NO-7491, Trondheim, Norway

April 26, 2022

Abstract

The role of the crystal lattice, temperature and magnetic field for the spin structure formation in the 2D van der Waals magnet Fe_5GeTe_2 is a key open question. Using Lorentz transmission electron microscopy, we experimentally observe topological spin structures up to room temperature in the metastable pre-cooling and stable post-cooling phase of Fe_5GeTe_2 . Over wide temperature and field ranges, skyrmionic magnetic bubbles form without preferred chirality, which is indicative of a centrosymmetric crystal structure. In the pre-cooling phase, these bubbles are observable even without the application of an external field, while in the post-cooling phase, a transformation from bubble domains to stripe domains is seen. To understand the magnetic order in Fe_5GeTe_2 we compare macroscopic magnetometry characterization results with microscopic

density functional theory calculation. Our results show that even up to room temperature, topological spin structures can be stabilized in centrosymmetric van der Waals magnets.

1 Introduction

Two-dimensional (2D) magnetic van der Waals (vdW) materials have seen rising attention since their recent introduction into the field of spintronics and beyond [1]. Many of these materials show promising properties for future applications, such as the semiconducting 2D ferromagnet CrI_3 [2], the metallic 2D ferromagnet Fe_3GeTe_2 [3] and the very recently discovered metallic 2D ferromagnet Fe_5GeTe_2 that orders even at relatively high temperatures [4]. The operation of a spintronic device requires ferromagnetic materials with room-temperature magnetic ordering, but most of the 2D vdW magnetic materials are either not ferromagnetic or do not possess a high ordering temperature. Here, Fe_5GeTe_2 is unique in that it has attracted specific scientific attention due to its room-temperature ferromagnetism with an ordering temperature of $T_C \approx 310$ K. To make use of a magnetic system for applications, spin structures are often required as information carriers. Interest in the dynamics of spin structures accordingly motivated recent studies on domain walls in vdW magnets [5, 6]. A particularly promising and exciting spin structure is the magnetic skyrmion [7–9]. So for 2D magnet applications, the required next step is the observation of topological magnetic spin structures near room temperature in Fe_5GeTe_2 . Fe_5GeTe_2 is additionally intriguing as it exhibits a phase transition at ≈ 100 K when it is first synthesized in a metastable phase [10]. So there is particular interest in the spin structures in a Fe_5GeTe_2 crystal, before and after going through the irreversible first-order phase transition upon cooling below $T \approx 100$ K. These phases are termed the metastable pre-cooling and the stable post-cooling phases. Real space probing of the crystal lattice and spin structure in both of these phases is still a major open question.

In the present work, bulk magnetic properties in the phases of 2D Fe_5GeTe_2 are characterized using a superconducting quantum interference device (SQUID), in combination with magnetic domain images using Lorentz transmission electron microscopy (L-TEM), which reveals stable topological spin structures up to room temperature. Further, the crystallographic space groups previously suggested for Fe_5GeTe_2 are investigated and we resolve open questions about their symmetry by presenting a spin chirality analysis. The spin chirality analysis involves careful considerations of the chirality of observed spin structures in Fe_5GeTe_2 , in order to deduce if the chiral Dzyaloshinskii–Moriya interaction (DMI) is present in the sample. Finally, the magnetic ordering of Fe_5GeTe_2 is investigated closely and we determine whether or not the system is in a spin glassy state. This is done via a careful comparison of the effective anisotropy obtained on a macroscopic scale with the effective anisotropy obtained on a microscopic scale.

2 Results and Discussion

2.1 Structural and composition analysis

Fig. 1(a) is a cross-section atomic resolution HAADF STEM image of the single-crystal Fe_5GeTe_2 used in the present work. Fig. 1(b) is a color-coded composition map obtained using EDX, which shows the periodic distribution of iron, germanium and tellurium. 2D layers consist of a sandwich of two planes of Te (brightest columns) with Ge and Fe planes located in-between. The layers are stacked along the c -axis and are approximately 1 nm thick including the vdW gap (dark area between two neighboring Te planes). A schematic model of the atomic structure is overlaid in the middle of Fig. 1(a) with the same color code as in Fig. 1(b). Following the notation used in Ref. [4], the Fe(2) and Fe(3) columns can be identified but the Fe(1) columns are not visible. Since STEM images show a projection of the crystal structure over the thickness of the lamella, this iron site is not easily visible because of its split-site nature [4]. Fig. 1(c) is another HAADF STEM that shows the presence of a stacking fault as indicated by red lines and an arrow, which has been previously reported in Fe_5GeTe_2 [11]. Here, stacking faults were observed primarily near the surface of the crystal (down to 200 nm below the surface). They are scarce deeper in the bulk of the sample, which has essentially a regular crystal structure, as shown in Fig. 1(a). Fig. 1(d) is a plan-view image where the c -axis is perpendicular to the image, which shows the hexagonal shape of the lattice.

2.2 Magnetic imaging of skyrmionic spin structures

We first observe the magnetization configuration at room temperature in our sample, as the type of spin structure also entails information about the underlying crystal structure of Fe_5GeTe_2 . The space group of Fe_5GeTe_2 has not so far been identified unambiguously. Li et al. and May et al. report the centrosymmetric space group $R\bar{3}m$ (No. 166) [4, 12], whereas Stahl et al. reported the non-centrosymmetric space group $R3m$ (No. 160) [11]. Here we consider the skyrmionic spin structures in Fe_5GeTe_2 to resolve this space group issue. A prerequisite for chiral spin structures, such as skyrmions and chiral domain walls, is the DMI, which occurs in systems with broken inversion symmetry [13]. In this regard, chiral spin structures would not be stabilized in bulk Fe_5GeTe_2 if its space group is $R\bar{3}m$, whereas they could be stabilized in bulk Fe_5GeTe_2 with the non-centrosymmetric space group $R3m$.

Fig. 2(a, b) show an in-focus phase shift image and the corresponding magnetic induction map reconstructed from an off-axis electron hologram obtained in a lamella cut perpendicular to the c -axis. The sample is magnetized along the crystallographic c -axis, which can also be deduced from SQUID measurements, as discussed in section S1 of the supplementary information. Two different types of circular spin structures can be observed. These bubbles with a black or white electron phase contrast correspond to type-I bubbles with a clockwise or counter-clockwise field rotation [14]. These two possible chiralities were found to occur with equal probabilities. Bubbles that show a black to white phase gradient correspond to topologically trivial type-II bubbles in which the rotation of the field changes [14]. Fig. 2(c) shows schematically the magnetic field in type-I and type-II bubbles. The presence of both type-II and type-I bubbles with two

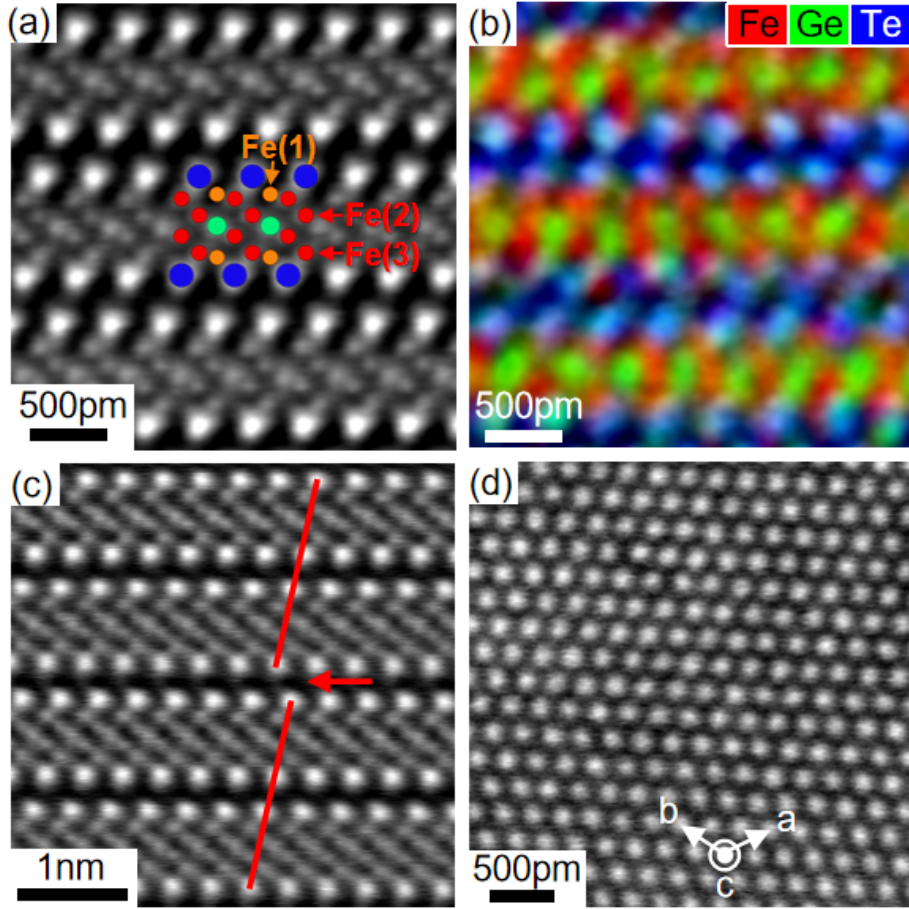


Figure 1: **High resolution analyses of the crystal structure of Fe_5GeTe_2 .** (a) High resolution HAADF STEM image of the structure with the c -axis along the vertical direction in the image plane. (b) Color-coded EDX composition map showing the distribution of iron, germanium and tellurium. A schematic model of the atomic structure is overlaid on image (a) with the same color code as in panel (b). (c) HAADF STEM image showing a stacking fault as indicated by red lines and an arrow. (d) HAADF STEM image of the structure with the c -axis perpendicular to the image plane.

possible chiralities indicate that they are not stabilized by DMI, but by dipolar interactions [15]. These observations are indicative of a centrosymmetric crystal structure and thus support the results of Li et al. and May et al. regarding the centrosymmetric space group $R\bar{3}m$ for Fe_5GeTe_2 [4, 12].

A series of Fresnel defocus images taken at different temperatures and external fields, as shown in Fig. 2(d), reveals that the formation of bubbles is favorable over labyrinth domains at larger applied fields, and that the bubbles form at fields slightly smaller than the saturating fields at any temperature. This is in line with previous results on other systems, where it was shown that skyrmion formation can be favorable at sufficiently strong external fields [16].

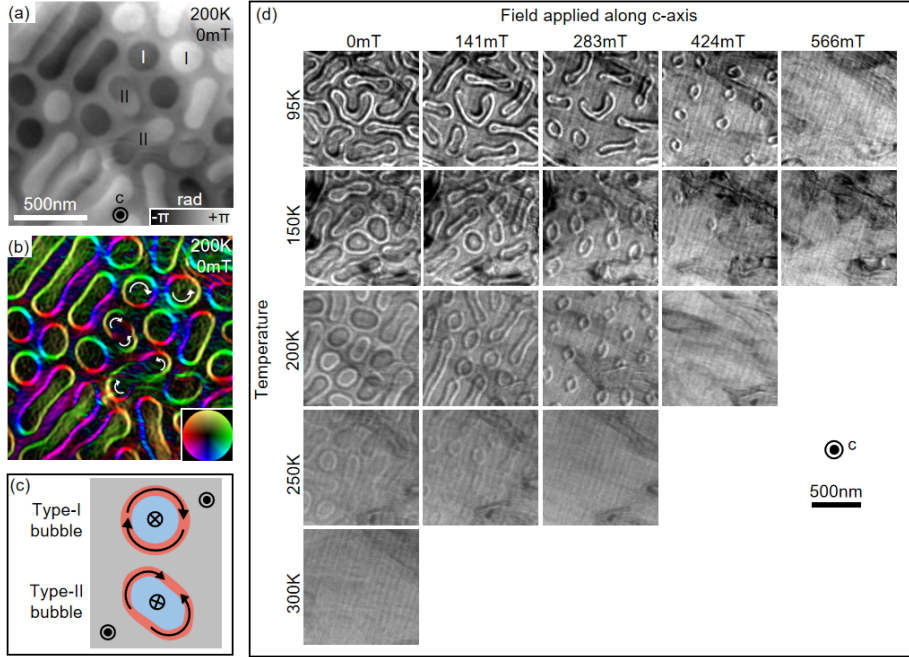


Figure 2: **Magnetic imaging of Fe_5GeTe_2 , revealing skyrmionic spin structures.** (a) phase shift image obtained using off-axis electron holography at $T = 200$ K and $B = 0$ mT in Fe_5GeTe_2 with the c -axis perpendicular to the image plane after previously applying out-of-plane fields up to $B = 566$ mT. (b) Corresponding color-coded magnetic induction map where the direction of the magnetic field is given by the color wheel in the bottom right corner. Type-II as well as Type-I bubbles with opposite winding numbers are present. (c) Schematic illustration of type-I and type-II bubbles. (d) Series of Fresnel images taken at various temperatures and external out-of-plane fields indicated in the figure, with a defocus of -1 mm, in a plan-view lamella (c -axis is perpendicular to the image plane). Bubbles form at higher external fields for lower temperatures.

Furthermore, we observe that the sizes of the magnetic bubbles shrink as the opposing net magnetization grows with external field, which is also in line with previous reports for chiral skyrmions and non-chiral skyrmions [14, 17].

2.3 Pre-cooling and post-cooling magnetic properties

In order to explore the bulk magnetic properties of Fe_5GeTe_2 in both the metastable pre-cooling and stable post-cooling phases, we have taken SQUID measurements of our sample while it is going through the phase transition. The temperature dependence of the magnetization for two magnetic field directions, B parallel to the ab -plane ($B_{ab\text{-plane}}$) and B parallel to the c -axis ($B_{c\text{-axis}}$) in an external field of 0.1 T for Fe_5GeTe_2 is shown in Fig. 3(a) and (b), respectively. For $B_{ab\text{-plane}}$, the first Field Cooled Cooling (FCC₁) curve reveals three magnetic anomalies. The anomaly at 271 K corresponds to the magnetic ordering temperature (T_C). The anomaly related to decreasing magnetization at 136 K

(T_{C2}) may correspond to a transition to a spin glassy phase [18]. Another possible explanation is that Fe_5GeTe_2 may be in a ferrimagnetic order under these conditions, as previously suggested for a similar temperature range by Ohta et al. and Alahmed et al., respectively [19, 20]. However, as soon as our sample reaches the stable post-cooling phase, it is found to be in a ferromagnetic state. Finally, the anomaly of a sudden increase in magnetization at $T = 87$ K corresponds to an irreversible magneto-structural phase transition (T_S) from a metastable pre-cooling phase to a stable post-cooling phase, consistent with previous results [4, 11]. In the Field Cooled Warming (FCW) curve and the second Field Cooled Cooling (FCC₂) curve, no such anomaly is evident at ≈ 100 K, thus confirming the 87 K anomaly of FCC₁ data was due to the non-reversible nature of this magneto-structural phase transition. While a weak anomaly with an increase in magnetization is evident at 118 K in FCW followed by a narrow hysteresis between FCW and FCC₂, it may be due to some spin reoriented phase transition. Further, the critical temperature T_C has shifted from 270 K to 310 K. Such a shift in T_C is consistent with previous reports [10]. The difference in the net magnetization between 100 K to 300 K for FCW and FCC₁ curves may be partially caused by the two different spin textures that Fe_5GeTe_2 exhibits between the stable post-cooling and the metastable pre-cooling phases, which will be discussed later in more detail.

Due to the irreversibility of the phase transition that occurs at 87 K, newly synthesized crystal pieces were chosen for the $B_{c\text{-axis}}$ measurements. The $B_{c\text{-axis}}$ data curves show similar magnetic behavior to that of the $B_{\text{ab-plane}}$ configuration. The slightly different values of T_{C2} and T_S for the $B_{\text{ab-plane}}$ and $B_{c\text{-axis}}$ FCC curves may be due to the different magneto-crystalline anisotropy. That T_C is almost the same value in both configurations further indicates that the magneto-crystalline anisotropy is a possible origin of the observed difference in T_{C2} and T_S for the two measurement configurations. The third and final curve is a zero-field cooled (ZFC) curve, which also shows a T_C of 310 K with low net magnetization. The large difference between the ZFC and FCW curves may have resulted from the occurrence of different domain configurations due to the external magnetic field-induced reorientation of ferromagnetic components.

In Fig. 4, one can quantitatively see an increase in magnetization in the post-cooling phase compared to the pre-cooling phase under otherwise equivalent conditions. This is true for the wide range of measured temperatures and external fields, in both the $B_{c\text{-axis}}$ and $B_{\text{ab-plane}}$ configurations. e.g. at 150 K and 100 mT in the $B_{\text{ab-plane}}$ configuration:

$$M_{\text{pre-cooling}}^{150\text{K}}(B = 100 \text{ mT}) = (5.75 \pm 0.12) \cdot 10^5 \text{ A m}^{-1}, \quad (1)$$

$$M_{\text{post-cooling}}^{150\text{K}}(B = 100 \text{ mT}) = (6.54 \pm 0.13) \cdot 10^5 \text{ A m}^{-1}. \quad (2)$$

The SQUID measurements yielded a saturation magnetization of

$$M_s = (8.12 \pm 0.16) \cdot 10^5 \text{ A m}^{-1}. \quad (3)$$

To confirm the validity of this saturation magnetization value, an independent method to determine the saturation magnetization via analysis of the stripe domain patterns is used [21]. The resulting value is $M_s = (2.56 \pm 1.40) \cdot 10^6 \text{ A m}^{-1}$. This value has a relatively large uncertainty, and the method neglects e.g. shape anisotropy and surface defects. However, it is sufficiently close

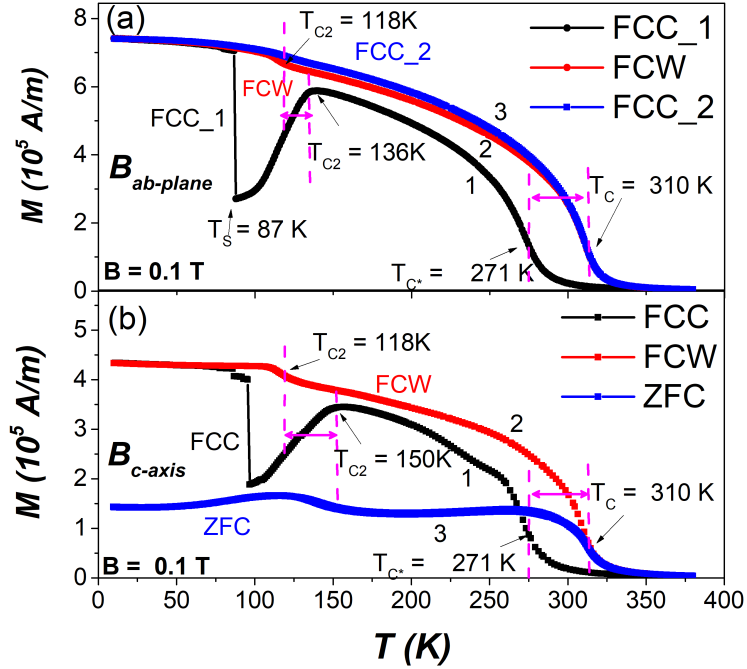


Figure 3: **Magnetization vs temperature of Fe_5GeTe_2 , where the external field B is applied along the c-axis and in the ab-plane with a field strength of 0.1 T.** Zero field cooled (ZFC) indicates that the sample was cooled without application of an external field and then the field of 0.1 T was applied at the lowest temperature followed by measurements performed during warming. FCC/FCW indicates measurements performed subsequently during cooling/warming with the field kept on, respectively. The numbers 1, 2, 3 defines the measurement sequence. When the external magnetic field is in the ab-plane, the sequence is FCC₁, followed by FCW & finally FCC₂, while for B along the c-axis, the sequence is FCC followed by FCW and finally ZFC.

to the saturation magnetization measured with the SQUID and thus confirms its validity. The details of the method and calculation can be found in section S2 of the supplementary information.

Finally, we have taken a series of Fresnel defocus images of our sample at temperatures ranging from 95 K to 290 K and at a constant external field of $B = 100$ mT, both in the pre-cooling and post-cooling phases. The phase transition from the metastable pre-cooling to the stable post-cooling phase in the TEM lamellas was achieved by cooling the sample down to ≈ 77 K, leaving it in liquid nitrogen for one hour. The images for these temperature sweeps are shown in Fig. 5. A striking difference between the two sets of images is that skyrmions are formed in the pre-cooling phase, but stripe domains form in the post-cooling phase, under otherwise equivalent circumstances. Since magnetic skyrmions predominantly form when an external field close to the saturation field is applied, this suggests that the saturation field of our sample has increased during the phase transition to the post-cooling phase. This could be explained

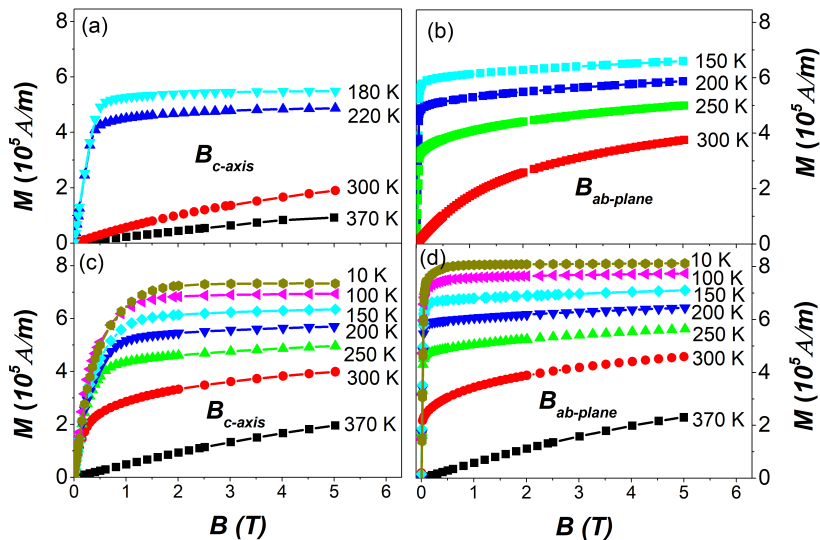


Figure 4: **The magnetic field dependent magnetization curves with the external field along the c-axis and in the ab-plane at different temperatures.** (a, b) for the pre-cooling and (c, d) for the post-cooling phase.

by an increase in the magnetization in the post-cooling state, as this would mean that the dipolar energy is still large relative to the external field contribution. Magnetometry measurements of a bulk sample using a SQUID support this idea, and yield larger magnetizations at moderate fields in the post-cooling phase compared to the pre-cooling phase, as discussed earlier in this subsection.

2.4 Magnetic ordering

It was shown in the previous subsection that Fe_5GeTe_2 shows a decrease in magnetization upon cooling from T_{C2} down to T_S while the sample is in the metastable pre-cooling phase (see Fig. 3), which indicates that Fe_5GeTe_2 might exhibit ferrimagnetic order or is in a spin glassy state. To distinguish these effects, we study next whether or not Fe_5GeTe_2 is in a glassy spin state. To this end, the micromagnetic anisotropy constant K is experimentally determined in two independent ways and compared. One method is to consider the hard-axis saturation field $B_{\text{sat}}^{\text{IP}}$, which is simply related to the exchange constant via the Stoner-Wohlfarth model [22]. By finding the total energy minimum with a given field applied along the hard-axis, and including Zeeman and anisotropy interactions, one finds that the expression for in-plane saturation is:

$$K_{\text{IP}} = B_{\text{sat}}^{\text{IP}} \frac{M_s}{2}. \quad (4)$$

A complementary approach to determine K is via the domain wall width δ [23]:

$$\delta = \pi \Delta = \pi \sqrt{\frac{A}{K_\delta}}, \quad (5)$$

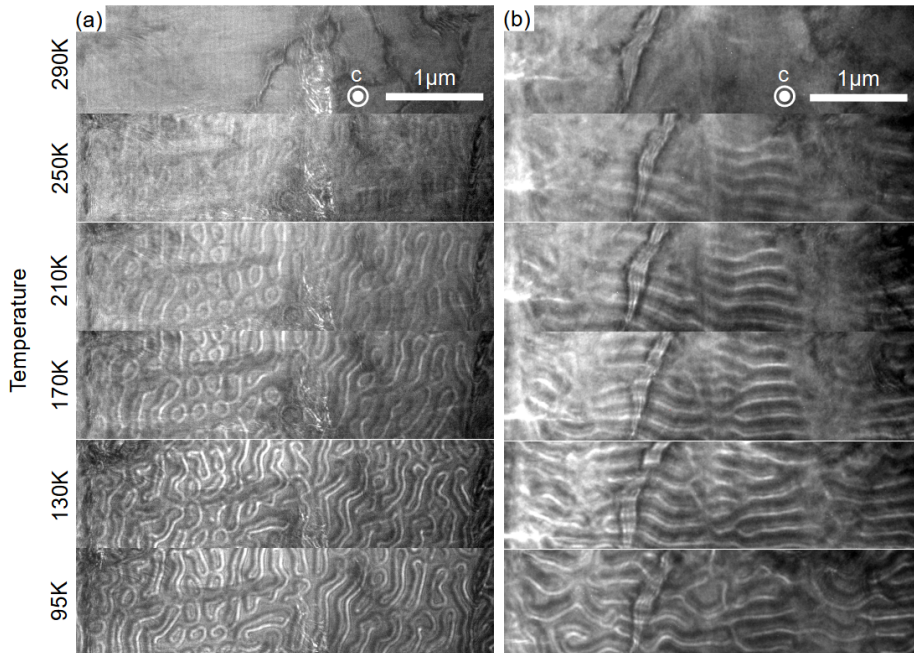


Figure 5: **Fresnel images of Fe_5GeTe_2 at various temperatures indicated in the figure and a constant external field of $B = 100 \text{ mT}$.** A defocus of -1 mm was used in a plan-view lamella (c -axis is perpendicular to the image plane), recorded before (a) and after (b) leaving the sample in liquid nitrogen for one hour.

where A is the micromagnetic exchange constant and Δ is a fit parameter used in the determination of the domain wall width δ from the measured domain wall profile. Note that when measuring K_{IP} , the quantities involved are determined on a macroscopic scale, whereas the determination of K_δ will require knowledge of the exchange interaction, which is short-ranged and dominates on the nanoscale. Thus, local disorder present in spin glasses [24] would manifest itself by affecting K_δ and K_{IP} differently.

To obtain K_δ , the micromagnetic exchange coupling constants were calculated using the JuKKR density functional theory (DFT) code [25] (see method section 4.4). This code employs the method of infinitesimal rotations [26, 27] to map the interactions among spins $\vec{S}_i = \vec{M}_i/\mu_i$ ($\mu_i = |\vec{M}_i|$) at lattice sites i onto the extended classical Heisenberg Hamiltonian

$$H = - \sum_{i \neq j} J_{ij} (\vec{S}_i \cdot \vec{S}_j) - \sum_{i \neq j} \vec{D}_{ij} \cdot (\vec{S}_i \times \vec{S}_j) - \sum_i K (\vec{S}_i \cdot \hat{e}_z)^2, \quad (6)$$

where the first term describes the exchange interaction, the second term represents DMI, and the final term describes the uniaxial out-of-plane anisotropy. The micromagnetic spin stiffness is

$$A = \frac{1}{2V} \sum_{i \neq j} J_{ij} r_{ij}^2, \quad (7)$$

where V is the volume per Fe atom, which can be calculated from the exchange coupling constants [27]. These parameters define the micromagnetic energy functional

$$E[\vec{m}] = \int d\vec{r} \left[A \dot{\vec{m}}^2 + K m_z^2 \right], \quad (8)$$

where the contribution of the spiralization that is related to the DMI vectors is neglected because it is found to vanish. The micromagnetic exchange constant obtained from this method is

$$A_{\text{DFT}} = 0.1508 \text{ eV nm}^{-1}. \quad (9)$$

An alternative, independent method to approximate the micromagnetic exchange constant A by considering the magnetic ordering temperature and crystal structure, is presented and executed in section S3 of the supplementary information. The result is $A_{\text{H}} = (0.060 \pm 0.007) \text{ eV nm}^{-1}$ and it is fairly close to the DFT value considering that many assumptions are made in this alternative method. Further calculations and comparisons to experiment, which support the DFT models and calculations are presented in the supplementary sections S4 and S5.

To determine the effective anisotropy K_{δ} using the spin stiffness A , we next need to determine the domain wall width δ . The domain wall parameter Δ can in principle be determined from phase shift images obtained using off-axis electron holography by fitting the magnetic phase gradient profile perpendicular to a domain wall and using the well-known theoretical profile $M_z^{\text{theo}}(x) = M_0 \cdot \tanh(x/\Delta)$. In reality the profiles will not be perfectly centered, so we use a fit function which allows for shifts:

$$M_z^{\text{fit}}(x) = M_0 \cdot \tanh((x - x_{\text{shift}})/\Delta) + M_{\text{shift}}, \quad (10)$$

where M_0 is the amplitude of the magnetization, x is the position perpendicular to the domain wall, and x_{shift} and M_{shift} are the free fit parameters accounting for imperfect centering. To obtain reliable results, each line drawn perpendicular to the domain walls has a width of 277.5 nm (300 pixels) to average across. An example of such a line is shown in Fig. 6(a), and the corresponding magnetic profile and fit is shown in panel (b). Overall, the domain wall width has been determined via four independent lines at 95 K and five different lines at 200 K. The resulting domain wall widths are $\delta^{95\text{K}} = (24.2 \pm 5.2) \text{ nm}$ and $\delta^{200\text{K}} = (36.3 \pm 3.5) \text{ nm}$. The uncertainties are estimated via the standard deviation of the domain wall widths obtained from all lines used at each temperature. Accordingly, the fit parameters are $\Delta = \delta/\pi$. Thus, all required parameters to find K_{δ} via equation 5 are known, and we find using A_{DFT} and the parameters Δ :

$$K_{\delta}^{95\text{K}} = (2.55 \pm 0.55) \cdot 10^{-3} \text{ eV nm}^{-3}, \quad (11)$$

$$K_{\delta}^{200\text{K}} = (1.13 \pm 0.11) \cdot 10^{-3} \text{ eV nm}^{-3}. \quad (12)$$

For the alternative determination of K via the saturation field along the hard-axis, images of the cross-section lamella sample are recorded at various field strengths at 95 K and 200 K (examples of images at 95 K are shown in Fig. 7(c-e)). The point at which the magnetic contrast completely vanishes as a function of magnetic field is approximated by splining the data for which there is magnetic contrast, and interpolating to the point where the minority domain has a width

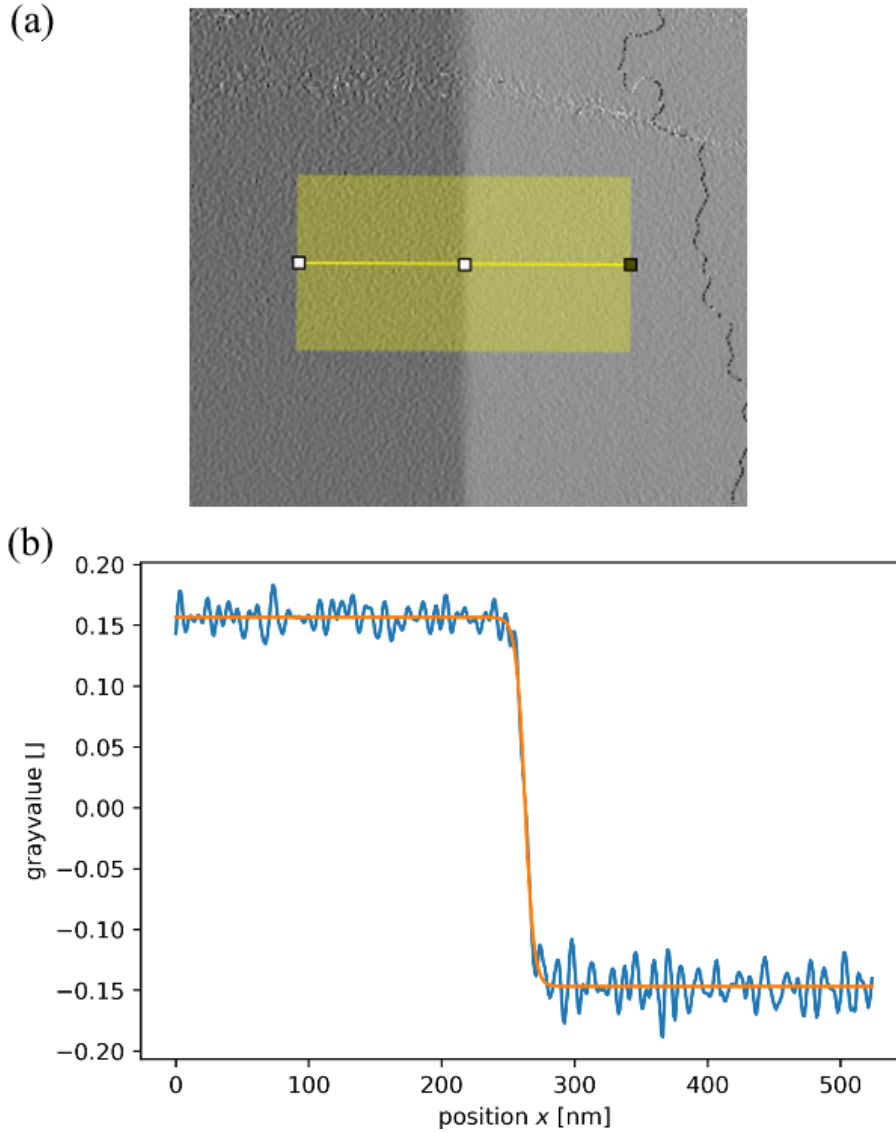


Figure 6: **Analysis of the magnetic contrast of a magnetic domain wall, with the aim to determine the domain wall width.** (a) Magnetic phase gradient image obtained using off-axis electron holography. A profile was extracted in the direction perpendicular to a 180° domain wall along the wide line. (b) Phase gradient profile (blue) and corresponding fit (orange). This example shows one magnetic profile across a domain wall at 95 K.

of zero. It should be noted that, since the field may not be applied perfectly perpendicular to the c -axis, this field is the monodomianization field, and serves as a lower bound for the hard-axis saturation field. However, it can be used as an estimation for the hard-axis saturation field. In this case, the saturation fields are estimated to be $B_{\text{sat}}^{\text{IP}, 95\text{K}} = (285 \pm 85) \text{ mT}$ and $B_{\text{sat}}^{\text{IP}, 200\text{K}} = (143 \pm$

43) mT. Accordingly, in conjunction with the saturation magnetization M_s from the SQUID measurements and inserting into equation 4, the micromagnetic anisotropy constants from this method are evaluated to be

$$K_{\text{IP}}^{95\text{K}} = (0.72 \pm 0.22) \cdot 10^{-3} \text{ eV nm}^{-3}, \quad (13)$$

$$K_{\text{IP}}^{200\text{K}} = (0.36 \pm 0.11) \cdot 10^{-3} \text{ eV nm}^{-3}. \quad (14)$$

Finally, the anisotropy constants obtained via both the domain wall and hard-axis saturation method can be compared. At 95 K the ratio between the effective anisotropy constants is $K_{\delta}^{95\text{K}}/K_{\text{IP}}^{95\text{K}} = 3.53 \pm 1.30$, and at 200 K it is $K_{\delta}^{200\text{K}}/K_{\text{IP}}^{200\text{K}} = 3.11 \pm 0.98$. Thus, the two methods to determine K used in this work, although they are completely independent and cover vastly different length scales, yield results which are on the same order of magnitude. The fact that the ratio K_{δ}/K_{IP} may systematically be larger than 1 could be attributed to the fundamental approximations used. Namely, since the hard-axis saturation field will be slightly larger than the monodomainization field, which we used to estimate the saturation field, K_{IP} should in reality be systematically slightly larger than the values we obtained. If the obtained anisotropy constants would differ by a large margin one could suggest that the material might be in a spin glassy state. But since they do not differ greatly, this analysis implies that the material is not in a spin glassy state. As such, this analysis in conjunction with the SQUID results indicates that Fe_5GeTe_2 might not be in a spin glassy state, but in a ferrimagnetic state while it is in the pre-cooling phase, as previously claimed [19, 20].

3 Conclusions

In conclusion, we have presented experimental observations of spin structures and magnetic properties in the promising 2D vdW magnet Fe_5GeTe_2 , to understand the magnetic ordering of this material. Notably, non-chiral magnetic skyrmions form in the material near room temperature when magnetic fields close to the saturation field are applied. The achirality of these magnetic bubbles suggests that there is no considerable DMI present in Fe_5GeTe_2 , which in turn supports the conclusion that Fe_5GeTe_2 has the centrosymmetric $R\bar{3}m$ crystal structure, rather than the otherwise proposed non-centrosymmetric $R3m$ crystal structure. Since Fe_5GeTe_2 exhibits a lower magnetization in the pre-cooling phase than in the post-cooling phase, we were able to observe bubbles at lower fields in the pre-cooling phase than in the post-cooling phase. Furthermore, by considering the anisotropy constants obtained via two independent methods, namely via the hard-axis saturation field and via the domain wall profile and predicted exchange constants, we conclude that Fe_5GeTe_2 is not in a spin glassy state. However, a notable drop of the magnetization with decreasing temperature observed in SQUID measurements suggests that Fe_5GeTe_2 is a ferrimagnet instead of a simple ferromagnet whilst in the pre-cooling phase. Future neutron diffraction experiments are required to fully ascertain the spin structure of Fe_5GeTe_2 . We have thus completed the necessary steps toward room temperature spintronics devices based on Skyrmion type spin structures, which are of significant interest for novel information storage and non-conventional computing concepts using 2D magnets.

4 Methods

4.1 A. Crystal synthesis

Single crystals of Fe_5GeTe_2 with an average size of $2 \times 2 \times 0.5 \text{ mm}^3$ were synthesized in quartz glass ampoules from the elements Fe, Ge, and Te in a 6 : 1 : 2 ratio in the presence of iodine as mineralizer. Similar to reference [4], Ge was supplied as a powder on the bottom of the quartz glass tube. Fe and Te were pressed to separate pellets of 1 mm diameter and positioned on top of the Ge powder without direct contact between the pellets. The reaction thus predominantly occurs through the gas phase and increases the single crystal size to several millimeters. The vacuum-sealed ampoules were heated up to 750 °C with 120 K/h and kept at this temperature for about 2 weeks before quenching them in room temperature water. The composition of the single crystals was confirmed by energy dispersive X-ray spectroscopy (Tescan SEM Vega TS 5130 MM equipped with a silicon drift detector, Oxford) with a ratio of Fe : Ge : Te of 4.72(5) : 1 : 1.94(4).

4.2 B. Lamella preparation

Electron transparent cross-section and plan-view lamellas were prepared using a 30 kV Ga^+ focused ion beam and scanning electron microscope (FIB-SEM) FEI Helios platform. The energy of the ion beam was decreased to 5 kV in the last steps of the thinning to minimize surface damage.

4.3 C. Transmission electron microscopy

Scanning transmission electron microscopy (STEM) and energy dispersive X-ray (EDX) spectroscopy were carried out using an FEI Titan TEM equipped with a Schottky field emission gun operated at 200 kV, a CEOS probe aberration corrector, a high angle annular dark-field detector (HAADF) and a Super-X EDX detection system [28]. Composition maps were obtained using the Thermo Scientific Velox software.

Magnetic imaging was carried out using Fresnel defocus and off-axis electron holography in an FEI Titan TEM equipped with a Schottky field emission gun, a CEOS image aberration corrector, a post-specimen electron biprism and a $4\text{k} \times 4\text{k}$ Gatan K2-IS direct detection camera [29]. A liquid-nitrogen-cooled specimen holder (Gatan model 636) was used to vary the sample temperature. The microscope was operated at 300 kV in magnetic field-free conditions (Lorentz mode) by using the first transfer lens of the aberration corrector as the primary imaging lens. The conventional objective lens was used to apply the chosen magnetic fields to the sample, which were pre-calibrated using a Hall probe. The field is applied along the electron beam direction *i.e.* perpendicular to the sample plane. For off-axis electron holography, the electron biprism was used to overlap a reference wave travelling in vacuum with an object wave passing through the sample. An elliptical illumination was used to optimize the coherence of the beam in the direction perpendicular to the biprism. The hologram width was 2.7 μm and the fringe spacing was 2.5 nm. Magnetic induction maps were reconstructed using Fourier transforms with the Holoworks plugin in the Digital Micrograph software (Gatan) [30]. The contribution of the mean inner

potential to the phase was removed by subtracting the phase of an hologram acquired above the Curie temperature.

4.4 D. DFT atomistic exchange tensor calculations

We performed density functional theory (DFT) calculations for bulk Fe_5GeTe_2 using the experimental lattice constants, $a = 4.04(2)\text{\AA}$, $c = 29.19(3)\text{\AA}$, from Ref. [4]. In order to account for the two Fe atoms at 50% occupancy we employed the use of the coherent potential approximation (CPA) [31]. We perform our calculations with the JuKKR code [25] which implements the full potential Korringa Kohn Rostoker (KKR) Green's Function method [31] with an exact description of the shape of the atomic cell [32, 33]. We use an angular momentum cutoff $l_{max} = 3$ and a generalised gradient approximation (GGA) to obtain the exchange-correlation potential [34]. Our calculations of the exchange coupling constants for the determination of the atomistic spin stiffness are based on the model of infinitesimal rotations [26, 27]. The domain wall widths calculated in the supplementary S5 are determined using the *Spirit* code [35].

5 Data Availability

All data used in the present work are available upon reasonable request.

6 Code Availability

All code used in the present work is available upon reasonable request.

References

1. Gibertini, M., Koperski, M., Morpurgo, A. F. & Novoselov, K. S. Magnetic 2D materials and heterostructures. *Nat. Nanotechnol.* **14**, 408–419 (2019).
2. Huang, B. *et al.* Layer-dependent ferromagnetism in a van der Waals crystal down to the monolayer limit. *Nature* **546**, 270–273 (2017).
3. Deng, Y. *et al.* Gate-tunable room-temperature ferromagnetism in two-dimensional Fe_3GeTe_2 . *Nature* **563**, 94–99 (2018).
4. May, A. F. *et al.* Ferromagnetism Near Room Temperature in the Cleavable van der Waals Crystal Fe_5GeTe_2 . *ACS Nano* **13**, 4436–4442 (2019).
5. Pei, K. *et al.* Controllable Domain Walls in Two-Dimensional Ferromagnetic Material Fe_3GeTe_2 Based on the Spin-Transfer Torque Effect. *ACS Nano* **15**, 19513–19521 (2021).
6. Purbawati, A. *et al.* In-Plane Magnetic Domains and Néel-like Domain Walls in Thin Flakes of the Room Temperature CrTe_2 Van der Waals Ferromagnet. *ACS Appl. Mater. Interfaces* **12**, 30702–30710 (2020).
7. Fert, A., Reyren, N. & Cros, V. Magnetic skyrmions: advances in physics and potential applications. *Nat. Rev. Mater.* **2**, 17031 (2017).

8. Everschor-Sitte, K., Masell, J., Reeve, R. M. & Kläui, M. Perspective: Magnetic skyrmions—Overview of recent progress in an active research field. *J. Appl. Phys.* **124**, 240901 (2018).
9. Tokura, Y. & Kanazawa, N. Magnetic Skyrmion Materials. *Chem. Rev.* **121**, 2857–2897 (2021).
10. May, A. F., Bridges, C. A. & McGuire, M. A. Physical properties and thermal stability of $\text{Fe}_{5-x}\text{GeTe}_2$ single crystals. *Phys. Rev. Mater.* **3**, 104401 (2019).
11. Stahl, J., Shlaen, E. & Johrendt, D. The van der Waals Ferromagnets $\text{Fe}_{5-d}\text{GeTe}_2$ and $\text{Fe}_{5-d-x}\text{Ni}_x\text{GeTe}_2$ - Crystal Structure, Stacking Faults, and Magnetic Properties. *Z. Anorg. Allg. Chem.* **644**, 1923–1929 (2018).
12. Li, Z. *et al.* Magnetic critical behavior of the van der Waals Fe_5GeTe_2 crystal with near room temperature ferromagnetism. *Sci. Rep.* **10**, 15345 (2020).
13. Manchon, A. & Belabbes, A. Spin-Orbitronics at Transition Metal Interfaces. *Solid State Physics* **68** (eds Stamps, R. L. & Camley, R. E.) 1–89 (2017).
14. Loudon, J. C. *et al.* Do Images of Biskyrmions Show Type-II Bubbles? *Adv. Mater.* **31**, e1806598 (2019).
15. Yokota, T. Numerical Investigation of Magnetic Bubble Types in a Two-Dimensional Ferromagnetic System with Dipole–Dipole Interactions. *J. Phys. Soc. Japan* **88**, 084702 (2019).
16. Lemesh, I. *et al.* Current-Induced Skyrmion Generation through Morphological Thermal Transitions in Chiral Ferromagnetic Heterostructures. *Adv. Mater.* **30**, e1805461 (2018).
17. Woo, S. *et al.* Observation of room-temperature magnetic skyrmions and their current-driven dynamics in ultrathin metallic ferromagnets. *Nat. Mater.* **15**, 501–506 (2016).
18. Mathieu, R., Jönsson, P., Nam, D. N. H. & Nordblad, P. Memory and superposition in a spin glass. *Phys. Rev. B* **63**, 092401 (2001).
19. Alahmed, L. *et al.* Magnetism and spin dynamics in room-temperature van der Waals magnet Fe_5GeTe_2 . *2D Mater.* **8**, 045030 (2021).
20. Ohta, T. *et al.* Enhancement of coercive field in atomically-thin quenched Fe_5GeTe_2 . *Appl. Phys. Express* **13**, 043005 (2020).
21. Johansen, T. H., Pan, A. V. & Galperin, Y. M. Exact asymptotic behavior of magnetic stripe domain arrays. *Phys. Rev. B* **87**, 060402 (2013).
22. Stoner, E. C. & Wohlfarth, E. A mechanism of magnetic hysteresis in heterogeneous alloys. *Philos. Trans. Royal Soc. A* **240**, 599–642 (1948).
23. Heide, M., Bihlmayer, G. & Blügel, S. Dzyaloshinskii-Moriya interaction accounting for the orientation of magnetic domains in ultrathin films: $\text{Fe}/\text{W}(110)$. *Phys. Rev. B* **78**, 140403 (Oct. 2008).
24. Sherrington, D. & Kirkpatrick, S. Solvable Model of a Spin-Glass. *Phys. Rev. Lett.* **35**, 1792–1796 (1975).
25. The JuKKR developers. *The Jülich KKR Codes* <https://jukkr.fz-juelich.de>. 2021.

26. Liechtenstein, A., Katsnelson, M., Antropov, V. & Gubanov, V. Local spin density functional approach to the theory of exchange interactions in ferromagnetic metals and alloys. *J. Magn. Magn. Mater.* **67**, 65–74 (1987).
27. Schweffinghaus, B., Zimmermann, B., Heide, M., Bihlmayer, G. & Blügel, S. Role of Dzyaloshinskii-Moriya interaction for magnetism in transition-metal chains at Pt step edges. *Phys. Rev. B* **94**, 024403 (2016).
28. Kovács, A., Schierholz, R. & Tillmann, K. FEI Titan G2 80-200 CREWLEY. *Journal of large-scale research facilities JLSRF* **2** (2016).
29. Boothroyd, C., Kovács, A. & Tillmann, K. FEI Titan G2 60-300 HOLO. *Journal of large-scale research facilities JLSRF* **2** (2016).
30. Völkl, E., Allard, L. F. & Frost, B. A software package for the processing and reconstruction of electron holograms. *J. Microsc.* **180**, 39–50 (1995).
31. Ebert, H., Ködderitzsch, D. & Minár, J. Calculating condensed matter properties using the KKR-Green’s function method - Recent developments and applications. *Reports Prog. Phys.* **74**, 096501 (2011).
32. Stefanou, N., Akai, H. & Zeller, R. An efficient numerical method to calculate shape truncation functions for Wigner-Seitz atomic polyhedra. *Comput. Phys. Commun.* **60**, 231–238 (1990).
33. Stefanou, N. & Zeller, R. Calculation of shape-truncation functions for Voronoi polyhedra. *J. Phys. Condens. Matter* **3**, 7599–7606 (1991).
34. Perdew, J. P., Burke, K. & Ernzerhof, M. Generalized Gradient Approximation Made Simple. *Phys. Rev. Lett.* **77**, 3865–3868 (1996).
35. Müller, G. P. *et al.* Spirit: Multifunctional framework for atomistic spin simulations. *Phys. Rev. B* **99**, 224414 (2019).
36. Evans, R. F. L. *et al.* Atomistic spin model simulations of magnetic nanomaterials. *J. Phys. Condens. Matter* **26**, 103202 (2014).
37. Garanin, D. A. Self-consistent Gaussian approximation for classical spin systems: Thermodynamics. *Phys. Rev. B* **53**, 11593–11605 (1996).
38. Skubic, B., Hellsvik, J., Nordström, L. & Eriksson, O. A method for atomistic spin dynamics simulations: implementation and examples. *J. Phys. Condens. Matter* **20**, 315203 (July 2008).

7 Acknowledgements

The work at JGU Mainz was funded by the Deutsche Forschungsgemeinschaft (DFG, German Research Foundation) - TRR 173 - 268565370 (projects A01 and B02), project 403502522 (SPP 2137 skyrmionics) the EU (FET-Open grant agreement no. 863155 (s-Nebula)), and the Research Council of Norway (QuSpin Center 262633). The work at JGU Mainz and FZJ was funded by ERC Synergy grant agreement no. 856538 (3D MAGiC), T.S., P.R., S.B. and Y.M. gratefully acknowledge the Jülich Supercomputing Centre for providing computational resources and Deutsche Forschungsgemeinschaft (DFG, German Research Foundation) - TRR 173 - 268565370 (project A11), TRR 288 - 422213477 (project B06). T.G.S. Would like to thank Dr. Sarah Jenkins and Dr. Fabian Lux for fruitful discussions.

8 Author Information

8.1 Affiliations

Johannes Gutenberg Universität Mainz, Institut für Physik, Staudingerweg 7, 55128 Mainz, Germany

Maurice Schmitt, Tom G. Saunderson, Aga Shahee & Mathias Kläui

Ernst Ruska Centre for Microscopy and Spectroscopy with Electrons and Peter Grünberg Institute, Forschungszentrum Jülich, 52425 Jülich, Germany

Thibaud Denneulin, András Kovács & Amir Tavabi

Forschungszentrum Jülich GmbH, Wilhelm-Johnen-Straße, 52428 Jülich, Germany

Philipp Rübmann, Yuriy Mokrousov & Stefan Blügel

Max Planck Institute for Solid State Research, Heisenbergstraße 1, 70569 Stuttgart, Germany

Tanja Scholz, Bettina Lotsch

University of Bristol, School of Physics, HH Wills Physics Laboratory, Tyndall Avenue, Bristol BS8 1TL

Martin Gradhand

National and Kapodistrian University of Athens, Department of Physics, University Campus, GR-157 84 Zografou, Athens

Phivos Mavropoulos

8.2 Contributions

Tanja Scholz synthesized all Fe_5GeTe_2 samples used in the present work. Thibaud Denneulin prepared the TEM lamellas and conducted the LTEM experiments with the help of Amir Tavabi. András Kovács carried out the STEM and EDX measurements. Aga Shahee conducted the SQUID measurements. Tom G. Saunderson and Philipp Rübmann contributed equally to the DFT results. Martin Gradhand and Phivos Mavropoulos helped with the determination of the spin stiffness via T_C . Phivos Mavropoulos provided the theoretical T_C of Fe_5GeTe_2 based on DFT results. Maurice Schmitt analyzed the experimental and theoretical results to yield insights into the spin ordering of Fe_5GeTe_2 , and wrote the paper with Mathias Kläui. Bettina Lotsch supervised the synthesization of the Fe_5GeTe_2 crystals. Yuriy Mokrousov and Stefan Blügel discussed and supervised the DFT work. Mathias Kläui supervised the experimental SQUID measurements and devised the study. All authors commented on the results and contributed to the manuscript.

9 Ethics declarations

9.1 Conflict of Interest

The Authors declare that there is no conflict of interest.

10 Supplementary information

10.1 S1 Magnetic anisotropy in Fe_5GeTe_2

Isothermal magnetization vs. magnetic field (M vs. H) curves measured using a SQUID, under the applied field either parallel to the c -axis ($B_{c\text{-axis}}$) or the ab plane ($B_{ab\text{-plane}}$) are shown in Fig. 4 of the main text. Fig. 4(a) and (b) are for the pre-cooling phase and Fig. 4(c) and (d) for the post-cooling phase respectively. These magnetization curves are presented without taking into consideration the demagnetization factor, which plays a great role in defining the internal field in 2D flake-like and 1D needle-like crystals. These M vs. H curves indicate a soft ferromagnetic nature of both the pre-cooling and post-cooling phases with a weak magneto-crystalline anisotropy. The raw data indicates a smaller external field is needed to saturate magnetization in the ab -plane than along the c -axis, which may at first indicate that Fe_5GeTe_2 is an easy plane ferromagnet. However, consideration of the large contribution to internal field from the demagnetization factor for the c -axis configuration indicates an opposite behavior, where spins prefer to align along the c -axis, as has been reported by May et al. [4].

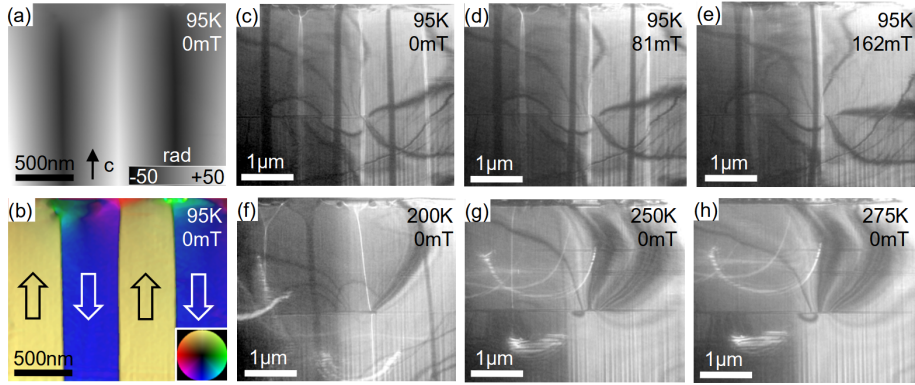


Figure 7: **L-TEM images of a Fe_5GeTe_2 lamella with the crystallographic c -axis in the image plane.** (a) phase shift image obtained using off-axis electron holography at 95 K and 0 mT in a cross-section lamella (c -axis is vertical in the image plane). (b) Corresponding color-coded magnetic induction map where the direction of the magnetic field is given by the color wheel in the bottom right corner. (c-e) Fresnel images obtained at 95 K and different external fields indicated on the images and with a defocus of -1 μm . (f-h) Fresnel images obtained at 0 mT and different temperatures indicated on the images.

Further, we investigated magnetic domains in lamellas cut from Fe_5GeTe_2 crystals parallel to the c -axis. Fig. 7(a,b) shows a phase shift image and the corresponding color-coded magnetic induction map obtained at 95 K and 0 mT. The presence of 180° stripe domains with domain walls (DWs) orientated along the $[001]$ direction confirm the easy-axis magnetic anisotropy of Fe_5GeTe_2 with the c -axis (001) as the easy-axis. Fig. 7(c-h) shows Fresnel defocus images obtained in the presence of different external fields applied nearly perpendicular

to the c -axis (0 to 162 mT) and at different temperatures (95 to 275 K). Even though the domain walls move in the presence of external fields and the width of the domains changes as a function of temperature, it can be observed that the DWs remain parallel to the c -axis even close to T_C at 250 K for instance, which confirms the easy-axis magnetic anisotropy of Fe_5GeTe_2 over a wide range of temperatures, which as shown in the main text, we have observed directly using L-TEM.

10.2 S2 Determination of the saturation magnetization from the stripe domain pattern

An independent way to determine the saturation magnetization is to closely examine the stripe domain patterns seen in the L-TEM images. This way, the validity of the SQUID results can be checked. According to theoretical considerations [21], the saturation magnetization of a film of magnetic material is given by

$$M_s = 2 \cdot \frac{a^2}{t} \cdot \frac{(B_c - B)/\mu_0}{\pi r_{\downarrow c}}, \quad (15)$$

where μ_0 is the magnetic vacuum permeability, M_s is the saturation magnetization, a is the overall domain periodicity, t is the film thickness, $r_{\downarrow c}$ is the width of the minority spin domains, and B and B_c are an arbitrarily chosen field and the saturating field, respectively. This theory assumes the considered sample is a magnetic film with uniaxial anisotropy and a large domain period, and considers exchange, Zeeman, anisotropy, and stray field energy contributions. The film thickness in our sample is not uniform, as scanning electron microscopy (SEM) measurements on various spots of the sample reveal. However, the measured local thicknesses all range from 90 nm to 210 nm, so the film thickness can be estimated to be $t = (150 \pm 60)$ nm. All other parameters on the right hand side of equation 15 can be estimated from the recorded TEM images. The domain periodicity a at the chosen field $B = 0$ mT can be estimated by adding the length of both blue lines in Fig. 8 and dividing by eight, since both blue lines together span a total of eight domain periods. The average length of the red lines is used to estimate $r_{\downarrow c}$. Since no magnetic contrast is visible at 655 mT anymore, the saturating field is estimated to be $B_c = (550 \pm 100)$ mT in this case. This method leads to a relatively large uncertainty in the minority domain width, since it is not only a relatively small distance to measure, but also because the measured widths cannot be measured exactly at the critical field. Therefore, each individual red line can be estimated to have an error of 50 %, which propagates to yield the average length of all lines of $r_{\downarrow c} = (53.6 \pm 10.2)$ nm. Via the same method, the domain periodicity is estimated to be $a = (272.1 \pm 96.5)$ nm.

Accordingly, using error propagation, the obtained saturation magnetization is $M_s = (2.56 \pm 1.52) \cdot 10^6$ A m⁻¹. Although this way the saturation magnetization has a larger relative uncertainty, its order of magnitude agrees with the values obtained from the SQUID measurements, thus confirming the validity of the SQUID measurements.

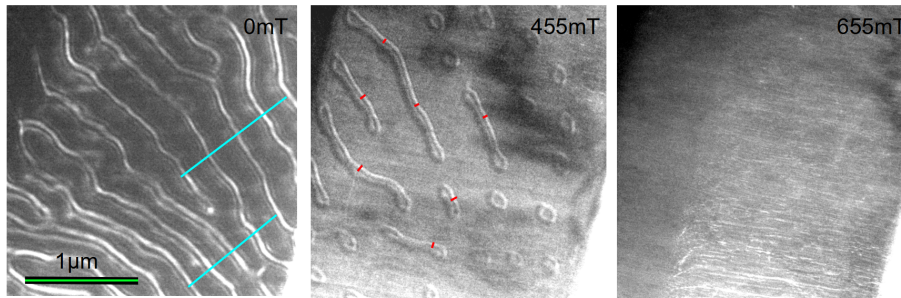


Figure 8: **L-TEM images of Fe_5GeTe_2 at 95 K.** The red lines are used to estimate the minority stripe domain width, whereas the blue lines are used to determine the overall domain periodicity. The green line is used to convert lengths in pixels to real lengths. The c -axis is perpendicular to the image plane.

10.3 S3 Determination of the micromagnetic exchange constant from the Curie temperature

To confirm the results obtained from DFT, the micromagnetic exchange constant (or spin stiffness) will be approximated in the following. To this end, one can invoke a simple Heisenberg model, which predicts in a mean-field approach [36]:

$$J_{\text{H}} = \frac{3kT_{\text{C}}}{2\epsilon z} \quad (16)$$

where k is the Boltzmann constant, T_{C} is the Curie temperature, z is the number of nearest neighbors in a unit cell and J_{H} is the Heisenberg exchange constant between magnetic sites. The parameter ϵ is a correction factor accounting for spin waves, which is slightly smaller than one and is well-known for common crystal structures [37]. Here, we will simply estimate $\epsilon = 0.8 \pm 0.1$. One can then find the micromagnetic exchange constant A_{H}^{IP} according to equation 7 by assuming $J_{ij} = J_{\text{H}}$ for nearest neighbors only and averaging the sum over nearest neighbors as well as the nearest neighbor distance squared $\overline{r_{ij}^2}$:

$$A_{\text{H}}^{\text{IP}} = J_{\text{H}} \cdot \frac{z \cdot \overline{r_{ij}^2}}{2V}, \quad (17)$$

with the volume per iron atom V . Combining 16 and 17 yields

$$A_{\text{H}}^{\text{IP}} = \frac{3kT_{\text{C}}}{4\epsilon} \cdot \frac{\overline{r_{ij}^2}}{V}, \quad (18)$$

The Curie temperature $T_{\text{C}} = (310 \pm 10)$ K can be estimated from the SQUID data. Note that in Fe_5GeTe_2 the Curie temperature changes depending on the thermal phase it is in. The larger value of $T_{\text{C}} = (310 \pm 10)$ K is valid for the post-cooling phase. The volume per magnetic site is $V = 0.0276 \text{ nm}^3$ according to the DFT results. For the mean squared neighbor distance, all neighbors in table 1 are considered and averaged over. Here, the split site nature of the Fe_1 site has to be considered, by weighting them only 50%. The result is $\overline{r_{ij}^2} \approx 0.06594 \text{ nm}^2$. Inserting these values into equation 18 yields

$$A_{\text{H}}^{\text{IP}} = (0.060 \pm 0.007) \text{ eV nm}^{-1}. \quad (19)$$

The value of the micromagnetic exchange constant obtained this way A_H is close to the value obtained via DFT A_{DFT} . Considering that many assumptions are made when calculating the micromagnetic exchange constant via the critical temperature due to the complex crystal structure of Fe_5GeTe_2 , the obtained value A_H turns out to be compatible with the more robust DFT result A_{DFT} and thus supports it.

type	Neighbor	Number of neighbors	Bond length
Fe ₁	Fe ₃	3	2.35464 Å
Fe ₁	Fe ₂	3	2.73786 Å
Fe ₂	Fe ₃	3	2.59186 Å
Fe ₂	Fe ₃	1	2.53864 Å
Fe ₂	Fe ₁	3	2.73786 Å
Fe ₃	Fe ₂	1	2.53864 Å
Fe ₃	Fe ₂	3	2.59186 Å
Fe ₃	Fe ₁	3	2.35464 Å

Table 1: The distances between individual iron sites in Fe_5GeTe_2 assuming the space group $R\bar{3}m$.

10.4 S4 Determination of T_C using the J_{ij} elements from DFT

In order to further confirm the validity of our DFT models and calculations, the critical temperature of Fe_5GeTe_2 has been determined by using both mean-field [36] and a Monte Carlo [38] methods.

In the mean-field method [36] we calculate two separate values for the Curie temperature. The first is an effective 2-dimensional Curie temperature, T_C^{2D} , which we obtain by extracting purely the intra-layer J_{ij} terms which yields $T_C^{2D} = 551$ K. The second is a bulk Curie temperature, T_C^{3D} , which additionally contains the inter-layer J_{ij} terms, yielding $T_C^{3D} = 871$ K. While the experimental samples used in the present work are more than 100 nm thick, T_C^{2D} might be more appropriate than T_C^{3D} , because ferromagnetic inter-layer coupling could be mediated by the long-range dipolar interaction. The Monte Carlo method, detailed in Ref. [38] yields a Curie temperature of $T_C^{\text{MC}} = 500$ K. This implies that the bulk Curie temperature is, as previously suggested, suppressed.

To conclude, using mean-field and Monte-Carlo methods we have determined three values for the T_C using the J_{ij} terms determined from *ab initio* methods. We conclude that it is more reasonable to assume the 2D mean-field value describes the system the best because inter-layer coupling could be mediated by the long-range dipolar interaction. The T_C determined from the Monte Carlo method is within a factor of 2 of the measured experimental T_C . As the independent determination of T_C through the J_{ij} terms is comparable to the experiment, it further justifies their use to determine K_δ in equations (11) and (12).

10.5 S5 Domain wall widths using the J_{ij} terms from DFT

To further analyse the determination of the exchange parameter A^{DFT} , we turn to atomistic simulations using the *Spirit* code to use the J_{ij} terms to accurately

determine a domain wall width. By simulating a domain wall we can further justify our use of A^{DFT} in the determination of the experimental value of K^δ . Firstly, we additionally determine K^{DFT} directly from the juKKR package giving a value of $K^{\text{DFT}} = 24 \cdot 10^{-3} \text{ eV nm}^{-3}$. This value is approximately a factor of 30 too large compared to experiment, however this quantity is determined from the bulk when in reality the domain wall is on the surface. This quantity can therefore be considered unknown and hence free to be determined. For our simulations we chose a $100 \times 20 \times 10$ supercell consisting of 200,000 spins in the simulation where periodic boundary conditions are chosen in \vec{b} and \vec{c} directions whereas open boundary conditions are used in the \vec{a} direction. The first and last plane of spins in the \vec{a} direction are then fixed in opposite ($\pm z$) directions which enforces a domain wall to form in the center of the simulation box. We solve the Landau-Lifshitz-Gilbert equation with the *Spirit* code [35] where the Depondt solver is applied for a maximum of 100,000 time steps with a maximal simulation time of 1000 ps to relax the magnetic texture. These simulations include the effect of temperature noise which is varied between 0 and 300 K. Fig. 9(a) is a plot of the domain wall width at 95 K for different choices of K^{DFT} within the range of experimental values of K . For large K the domain wall is shortened significantly compared to the experimental values and is hence not necessary to go beyond 0.7 meV/Fe. As the anisotropy constant decreases we see a rather flat distribution until 0.2 meV/Fe at which point the domain wall diverges for vanishing K . Choosing a particular value for $K = 0.04 \text{ meV/Fe}$ to match with the experimental value, Fig. 9(b) shows how the domain wall evolves as a function of temperature. We observe a steadily increasing value for the domain wall width with temperature, crossing $\delta = 23.2 \text{ nm}$ at 100K and $\delta = 27.7 \text{ nm}$ at 200K. This is in good agreement with experimentally determined domain walls when using the experimental anisotropy instead of the value determined by DFT which is more specific to the bulk. Three exemplary domain wall fit at temperatures of 20 K, 100 K and 300 K are shown in Fig. 10(a-c).

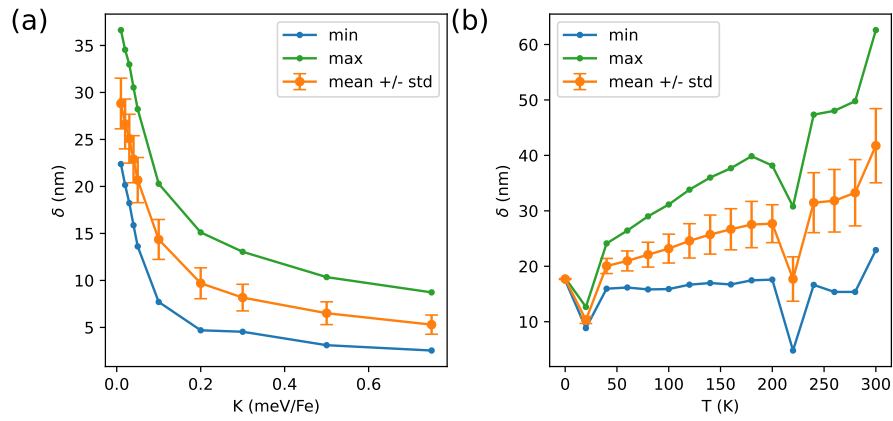


Figure 9: **Domain Wall widths using *ab initio* J_{ij} 's as a function of anisotropy and temperature.** (a) The domain wall width at 95 K as a function of anisotropy constant K . (b) The domain wall width with increasing temperature in the simulation. Green and blue lines are indicate the maximal and minimal determined values from the different lines of the Fe atom positions in the unit cell and among the multiple unit cell in the $200 \times 20 \times 10$ cell large supercell. The orange line gives the average over the 20×10 unit cell cross section parallel to the domain wall.

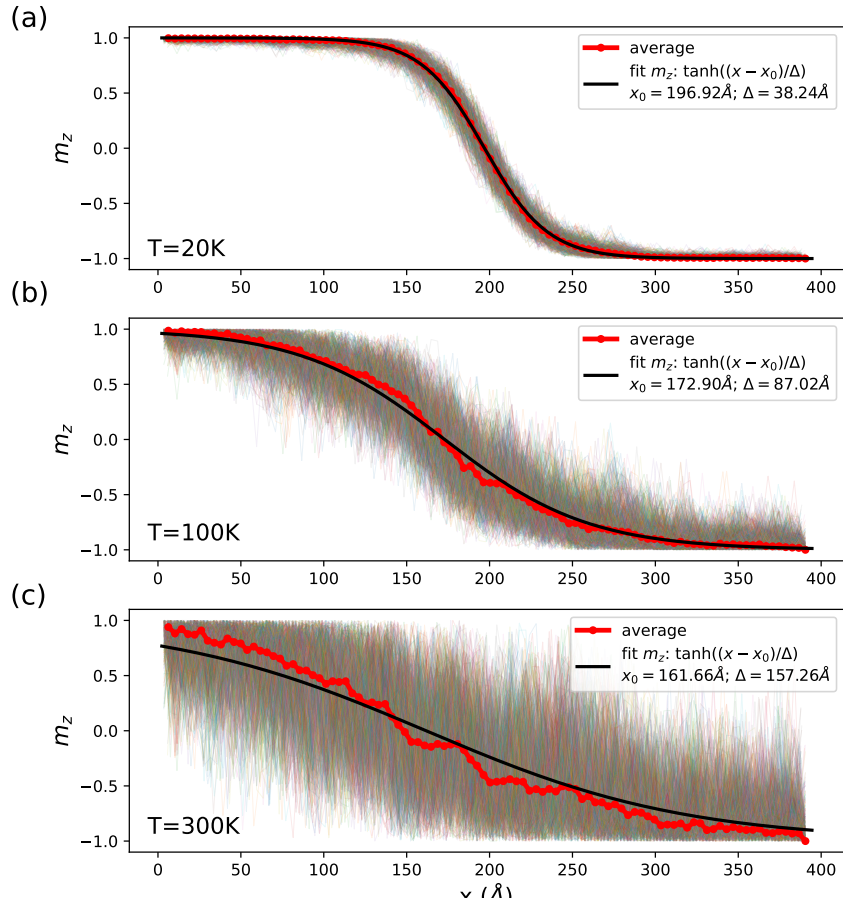


Figure 10: **Simulated domain Wall profiles.** (a-c) Profiles of the domain wall across all lines of Fe atoms in the 20×10 cell cross section of the Spirit supercell for increasing temperature of 20 K, 100 K and 300 K. The faint lines in the background are the individual line profiles where the temperature fluctuations are visible. The thick red lines show the average over the lines and the black line the fitted domain wall profile. The simulation uses the *ab initio* J_{ij} 's and the optimized value of the anisotropy of $K = 0.04$ eV/Fe. For large temperatures the fit starts to deviate from the average line (most visible in c) which is attributed to finite size effects in the simulation.